CHAPTER 9

Molecular Orbitals of Small Building Blocks

9.1 INTRODUCTION

In Section 7.5, we found it convenient to construct the molecular orbitals (MOs) of AH_2 by symmetry adaptation of bond orbitals. This analysis can easily be extended to other systems. Some bond orbitals may already transform as an irreducible representation of the molecular point group. It is usually only degenerate bond orbitals that require symmetry adaptation in constructing MOs. Of course, bond orbitals of the same symmetry can and will interact with each other, but these are details that for the most part will not be of concern in our qualitative analysis. In the following, we will first derive the MOs of AH, pyramidal AH_3, and tetrahedral AH_4 based upon the appropriate orbital interaction diagrams, and then analyze those MOs in terms of bond orbitals. As in **7.4b**, the hydrogen *s* orbital may be assumed to lie energetically in between the *s* and *p* orbitals of A. For convenience, the bond orbitals of AH, AH_3, and AH_4 may be constructed by assuming sp^3 hybridization on A.

9.2 THE AH SYSTEM

The interaction diagram for the orbitals of A and H is shown in Figure 9.1. The p_x and p_y orbitals of A do not overlap with the hydrogen *s* orbital, and so become the π set of nonbonding orbitals (**9.1**) for AH. According to the perturbation treatment of Chapter 3, $1\sigma^+$, $2\sigma^+$, and $3\sigma^+$ are derived as shown in **9.2**. In this MO description,

Orbital Interactions in Chemistry, Second Edition.
Thomas A. Albright, Jeremy K. Burdett, and Myung-Hwan Whangbo.
© 2013 John Wiley & Sons, Inc. Published 2013 by John Wiley & Sons, Inc.

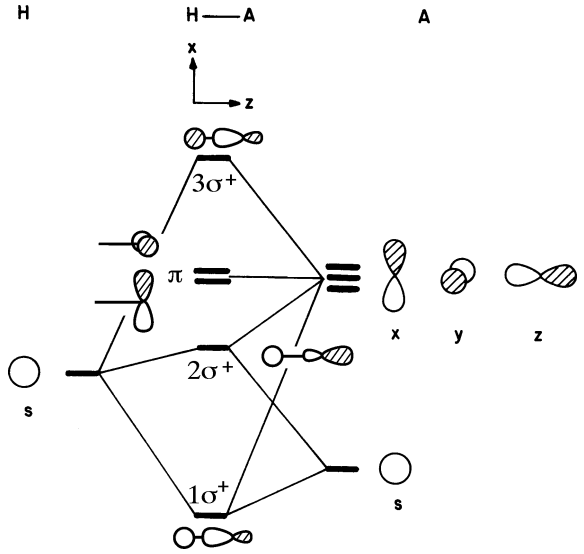

FIGURE 9.1
An orbital interaction diagram for AH.

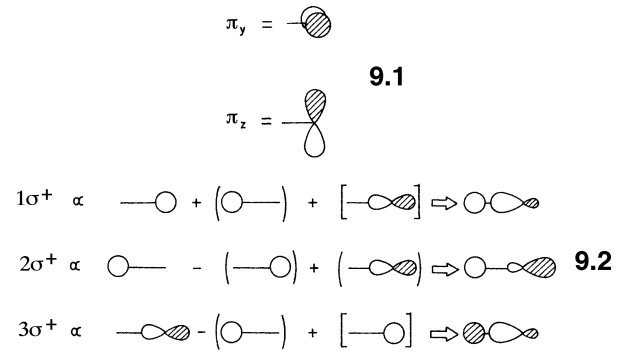

the second-order orbital mixing represented by brackets is essential for creating the orbital hybridization on A. One has the familiar three orbital pattern at work; $1\sigma^+$ and $3\sigma^+$ are the most bonding and antibonding HA combinations, respectively, possible. The middle orbital, $2\sigma^+$, is nonbonding and hybridized away from the HA region of space. The bond orbitals of AH that result from combining the sp^3 hybrid orbitals of A with a hydrogen *s* orbital are shown in Figure 9.2. One sp^3 hybrid orbital interacts with hydrogen *s* to form the σ_{AH} and σ^*_{AH} levels, and the remaining three

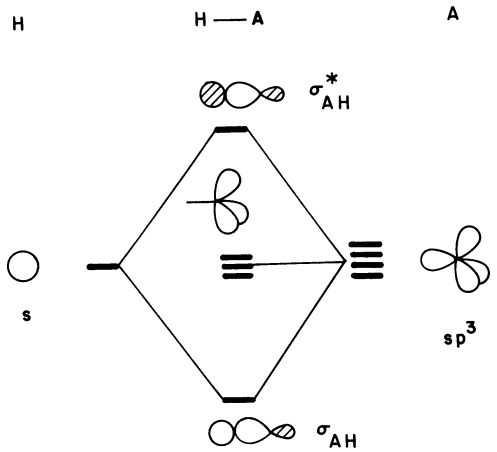

FIGURE 9.2
An orbital interaction diagram for AH using the bond orbital approach.

hybrid orbitals become nonbonding orbitals on A. Note that the bond orbitals σ_{AH} and σ^*_{AH} are already symmetry adapted (i.e., transform as one of the irreducible representations of the $C_{\infty v}$ point group), and thus are similar in character to the corresponding MOs $1\sigma^+$ and $3\sigma^+$, respectively. The three sp^3 nonbonding orbitals of A are not symmetry adapted in this sense, but a linear combination of them may be constructed as described in Section 4.5 to produce a set of symmetry-adapted MOs. Let us recall the vector decomposition of a hybrid orbital as exemplified in Section 6.2, and, for convenience of a graphical presentation, let us represent a hybrid orbital by showing only the large front lobe for the sp^3 hybrids. Then the MOs n_x, n_y, and n_σ may be approximated by the three sp^3 nonbonding orbitals as shown in **9.3**.

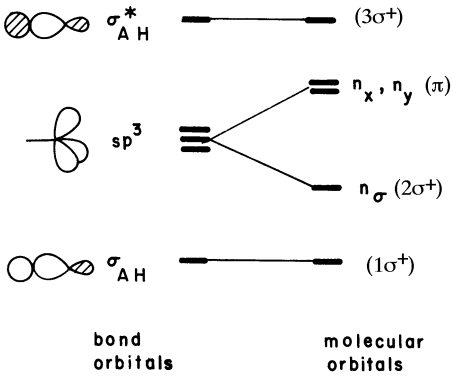

9.3

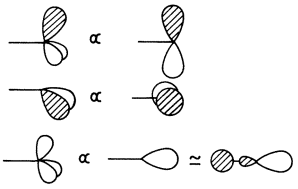

9.4

Consequently, the bond orbitals and MOs of AH are correlated as indicated in **9.4**. Notice the splitting of the three sp^3 hybrid orbitals into a degenerate pair and a single nondegenerate orbital, a result demanded by group theory. The σ^+ combination is the fully symmetric combination of the hybrids and the degenerate π set follows the familiar prescription shown in **9.3**. The π sets in **9.3** and **9.4** are exactly identical. From the delocalized LCAO approach, the $2\sigma^+$ molecular orbital has an atomic coefficient on hydrogen, whereas, the σ^+ combination of hybrids does not. This is due to the neglect of nondegenerate mixing with σ_{AH} and σ^*_{AH} (Figure 9.2). In this example, one could have just as easily started with sp^2 hybridization on A. The σ_{AH} and σ^*_{AH} combinations are formed from the one sp^2 hybrid pointed toward the hydrogen atom. Taking symmetry-adapted combinations of the other two hybrids yield a symmetric combination identical to $2\sigma^+$ and an antisymmetric combination that simplifies to an atomic p orbital on A, one member of the π set. The remaining p atomic orbital (AO) in this sp^2 hybridization scheme is, of course, the other component of the π set. An even easier bond orbital derivation for the orbitals of HA starts with sp hybridization at A. The combinations with the hydrogen s orbital give the same bonding/antibonding orbitals. Now one has an sp hybrid and two p AOs on A to represent the three nonbonding orbitals. The symmetry labels shown are correct, but is $2\sigma^+ sp^3$, sp^2, or sp hybridized on A? The amount of s character on A in $2\sigma^+$, as we shall see below, depends upon where A lies in the Periodic Table. That is, $1\sigma^+$, $2\sigma^+$, and $3\sigma^+$ always intermix in the bond orbital approach to yield a varying ratio of s/p character on A as well as s character on H.

The orbital derivation of AH was constructed assuming that the electronegativity of H and A are approximately equal. There are, of course, two other possible situations, which, following the derivation of AH_2 in Section 7.1, will create MOs with identical shapes, however, their weights at each center will not necessarily be the same. Figure 9.3 shows contour plots of the wavefunctions for HC and HF. These are calculations using STO-3G basis sets. The positive and negative values of

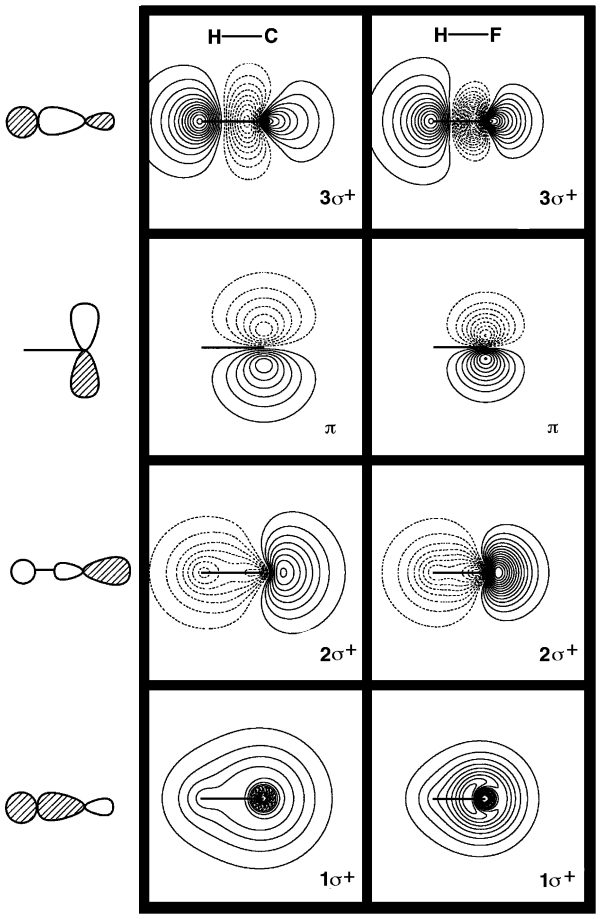

FIGURE 9.3
Contour plots of the wavefunctions for CH and HF. Only one component for the π sets is shown.

the wavefunctions are denoted by solid and dashed lines. The absolute value of each contour is one-half of the value of the contour before it proceeding from the nuclear regions outward. The gross similarity between the MOs of HC and HF underscore the idea that these orbitals do not change their shapes when the heavy atom is changed. The most obvious difference lies in the relative sizes of the AOs on carbon versus those for fluorine. Since fluorine is much more electronegative, the AOs are more contracted (e.g., compare the *p* AOs in the 1π set). The three σ^+ MOs for CH are more delocalized between C and H as implied by the interaction diagram in Figure 9.1. HF on the other hand corresponds to case **7.4c** and so $1\sigma^+$ is primarily F *s*. There is little *sp* hybridization in $2\sigma^+$, whereas, this feature is clearly present in CH. Finally, note that the amplitude on H for the $3\sigma^+$ MO is much greater for FH than it is for CH, a result demanded again by the electronegativity differences.

9.3 SHAPES OF AH_3 SYSTEMS

The interaction between the fragment orbitals of H_3 and the AOs of the central atom, A, shown in Figure 9.4 gives rise to the MOs of pyramidal AH_3 [1–4]. The p_x and p_y AOs on the A atom overlap and hence interact with the H_3 combination of e symmetry. A simple two-orbital interaction results. The $1e_x$ and $2e_x$ orbitals are the in-phase and out-of-phase combinations of e_x and p_x, respectively. Likewise, $1e_y$ and $2e_y$ are the in-phase and out-of-phase combinations of e_y and p_y, respectively. The $1a_1$,

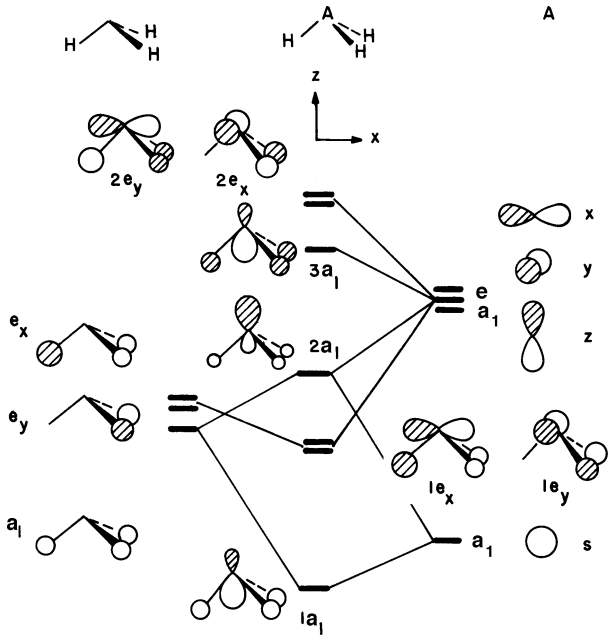

FIGURE 9.4
An orbital interaction diagram for pyramidal AH_3.

$2a_1$, and $3a_1$ molecular orbitals in Figure 9.4 are derived from the three orbital interaction between *s* and p_z on A with the H_3 combination of a_1 symmetry. The construction is illustrated in **9.5**. A pattern in common exists for the three a_1

9.5

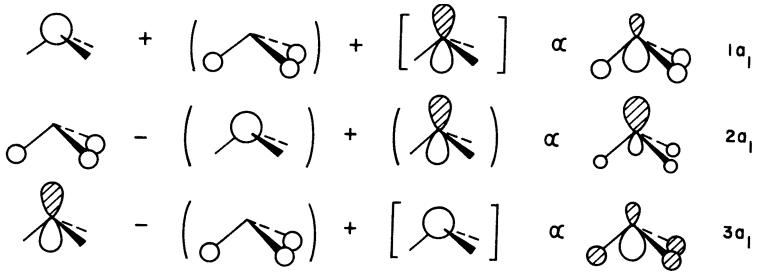

MOs we saw for AH_2 (**7.8**), AH (**9.2**), and AH_3 (**9.5**). The lowest and highest MOs of the three are always hybridized toward the hydrogen(s). The middle, nonbonding MO is concentrated on A and hybridized away from the hydrogen(s). This is a characteristic feature that we see again for the hypervalent molecules in Chapter 14 and the transition metal building blocks in Chapters 17–19. Whenever two different atomic orbitals on one center combine with an ensemble of hydrogen *s* or ligand σ donor orbitals, a maximally bonding combination at low energy and a maximally antibonding combination at high energy is produced. A nonbonding orbital at moderate energy is left behind, which is hybridized away from the surrounding hydrogens (or ligands). Contour plots of the valence molecular orbitals associated with NH_3 are given in Figure 9.5. The technical details are identical with those in Figures 9.3 and only the $1e_x$ and $2e_x$ components of the e sets have been plotted. Stylized representations of the molecular orbitals are drawn out on the lower left side of each plot. The hybridization in $2a_1$ is quite clear. There is much greater density (number of contours) on the top half of the molecule as compared to the region around the hydrogen atoms. The composition of $3a_1$, primarily a hydrogen *s* combination with nitrogen *p* mixed in an antibonding fashion, is in accord with our expectations of what this MO should look like given the greater electronegativity of

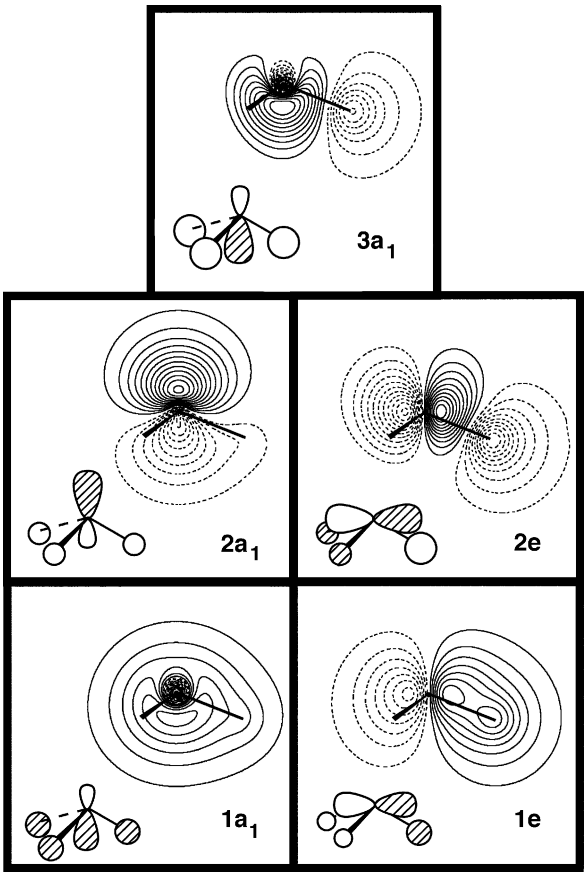

FIGURE 9.5
Contour plots of the valence molecular orbitals in NH_3. Only one member of each *e* set is shown.

nitrogen. It can be seen that the mixing of nitrogen *s* character produces hybridization toward the hydrogens in $1a_1$ and $3a_1$ as anticipated by **9.5**.

Formation of the bond orbitals of pyramidal AH_3 is shown in Figure 9.6. The bond orbitals σ_{AH} and σ^*_{AH} are not symmetry adapted since triply degenerate species

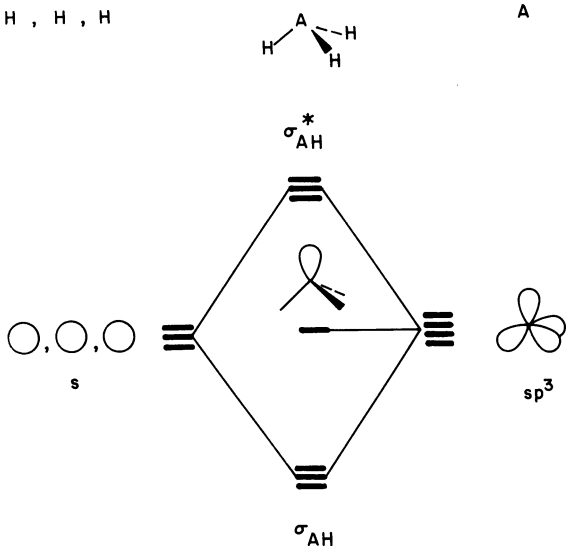

FIGURE 9.6
An orbital interaction diagram for pyramidal AH_3 in the bond orbital approach.

are not allowed in the C_{3v} point group. The main features of the MOs, $1a_1$, $1e_x$, and $1e_y$, are well approximated by the standard linear combinations in this case of the three σ_{AH} orbitals as in **9.6**. Similarly, the $3a_1$, $2e_x$, and $2e_y$ MOs are approximated in terms of the symmetry-adapted combinations of the three σ^*_{AH} orbitals. The sp^3 nonbonding

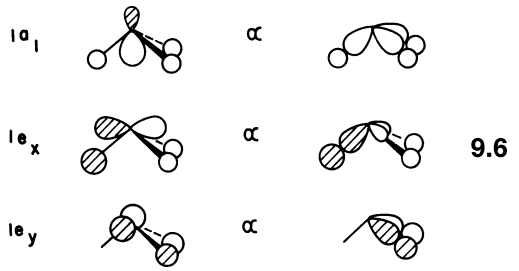

9.6

orbital is already symmetry adapted and similar in description to the $2a_1$ MO except for the absence of hydrogen *s* character. We could build this in by allowing it to interact with $1a_1$ and $3a_1$ symmetry-adapted combinations in a fashion identical to that used for the σ^+ set in the previous section. The energy of the nonbonding orbital does not change much as a result of this extra orbital mixing and remains concentrated on A. The degeneracy associated with the three σ_{AH} and σ^*_{AH} bond orbitals is broken after symmetry-adapted combinations are taken. The $1a_1$ combination of σ_{AH} is more stable than the 1*e* set since the latter contains appreciable *s* character on the A atom, whereas, the 1*e* set contains exclusively *p* character on A. Recall that atomic *s* orbitals lie lower in energy than *p*.

The MOs of trigonal planar AH_3 were already constructed by reference to the orbitals of H_3 and A in Figure 4.6. During the course of the trigonal planar to pyramidal (i.e., $D_{3h} \rightarrow C_{3v}$) distortion, the MO levels of AH_3 vary as shown in Figure 9.7. This Walsh diagram is derived from extended Hückel calculations for the PH_3 molecule. There is a break in the energy scale from about -14 eV to $\sim$0 eV. Let us use geometrical perturbation theory to analyze these results. Several trends in Figure 9.7 are immediately obvious. The $1a_1$ level is stabilized slightly upon pyramidalization since overlap between the hydrogen *s* orbitals increases. In other words at small H—P—H angles $e^{(1)}$ is negative. In the $1e'$ and $2e'$ levels, the magnitude of the overlap integral between the hydrogen *s* and *p* orbitals of P decreases upon pyramidalization, see Figure 1.5. Thus, the P—H bonding $1e'$ set rises in energy since $e^{(1)}$ is positive, and the P—H antibonding $2e'$ set correspondingly falls in energy since $e^{(1)}$ is negative. Recall that a similar situation occurred for the b_2 orbitals on bending in H_2S (see Section 7.3). The steeper slope associated with 2*e* is derived from the fact that there are larger atomic coefficients in 2*e* (this is an antibonding orbital) than there are in the 1*e* set. This, in turn, creates a larger value in absolute magnitude for $\tilde{S}_{ii}$ in 2*e* as compared to 1*e*. From first-order energy considerations, we expect both the $2a'_1$ and $1a'_1$ levels to go down slightly in energy and a''_2 to remain unchanged in energy. This clearly does not occur. Upon pyramidalization, both $2a'_1$ and a''_2 become orbitals of a_1 symmetry so the two may mix together. As a result $2a'_1$ is destabilized greatly on pyramidalization and a''_2 is stabilized. This orbital mixing will be examined in more detail below. For now, we note that the mixing of $2a'_1$ into a''_2 is always larger than the mixing of $1a'_1$ into a''_2 regardless of the identity of A. The rationale for this is precisely identical to the $1\sigma_g^+ - \pi_u - 2\sigma_g^+$ situation for bending in AH_2 discussed in Section 7.3.

Figure 9.7 shows that a six-electron AH_3 system such as CH_3^+ and BH_3 should be planar. The HOMO, $1e'$, of such a species is destabilized upon pyramidalization. The LUMO is the *p* orbital of A, which lies perpendicular to the molecular plane. Such an empty orbital, concentrated on one atomic center, is a powerful electron acceptor and is responsible for the Lewis acid character in boranes and carbocations.

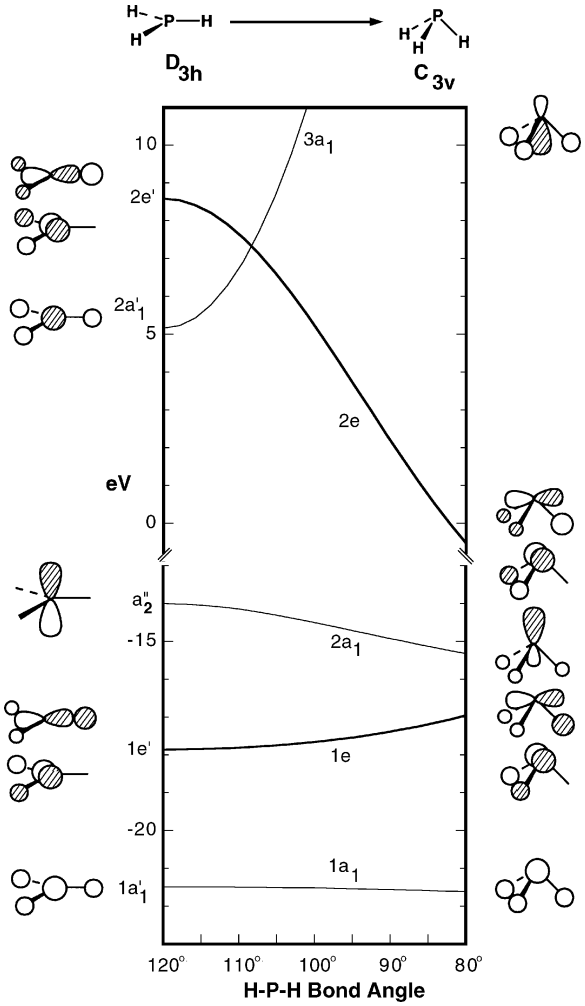

FIGURE 9.7
Walsh diagram for pyramidalization in PH_3. Notice the break in the energy scale.

Let us consider a nucleophilic addition to a carbocation CH_3^+ by representing a nucleophile, Nu:, by a filled nonbonding hybrid orbital n_σ. Figure 9.8 shows how n_σ is stabilized, primarily by a_2'', yielding the C—Nu bonding orbital σ. The resultant σ level is derived as in **9.7**. If the hydrogen atoms distort away from the incoming nucleophile,

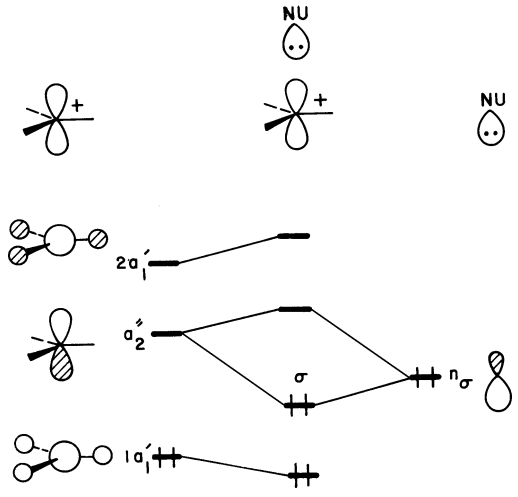

FIGURE 9.8
An orbital interaction diagram for the addition of a nucleophile to CH_3^+.

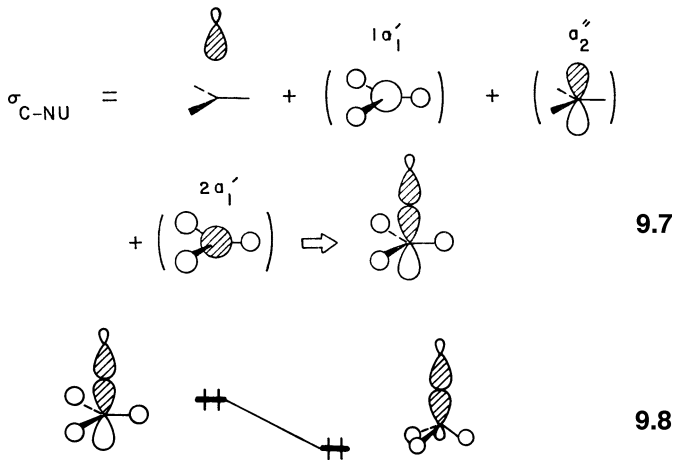

9.7

9.8

antibonding between the hydrogen *s* components in the a_1 orbitals and n_σ is decreased. Furthermore, bonding between the hydrogen *s* components in the a_1 orbitals and a_2'' is increased. So as shown in **9.8**, the σ orbital is further stabilized if the carbon configuration becomes tetrahedral. In another, equivalent context the orbital interaction shown in Figure 9.8 serves to transfer electron density from n_σ to a_2'', which induces the geometrical response (i.e., pyramidalization) of the CH_3 moiety since the $2a_1$ MO is stabilized on pyramidalization (see Figure 9.7).

It is of interest to consider the formation of diborane, B_2H_6, **9.9**, in terms of the HOMO and LUMO of two BH_3 fragments. The most stable arrangement of two BH_3 units in the incipient stage of dimerization is given by **9.10**, which maximizes the extent of the two HOMO-LUMO interactions **9.11**. On dimerization, a

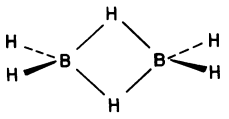

9.9

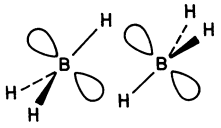

9.10

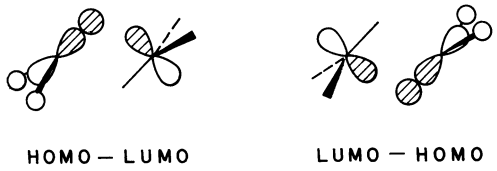

9.11

pyramidalization occurs at each BH_3 unit. This takes place via a mechanism exactly analogous to the one considered in Figure 9.8. Here, electron transfer takes place from one component of the le′ orbital (**9.11**). One would predict that decreasing the B–H distance for the bridging borohydride bonds should smoothly result in pyramidalization at boron.

Figure 9.7 shows that an eight-electron AH_3 system such as CH_3^- or NH_3 should be pyramidal since now the a_2'' orbital is filled and it is markedly stabilized upon pyramidalization. The resultant HOMO in the new geometry ($2a_1$) resembles an sp^3 nonbonding orbital. The potential energy diagram for pyramidal inversion in an eight-electron AH_3 system will be one where the two mirror image pyramidal geometries are minima and the planar species is a transition state that interconnects

TABLE 9.1 The R—A—R Bond Angles and Inversion Barriers for Some R_3A Molecules

	H_3A		Me_3A	F_3A		H_3A	
A	H—A—H	ΔE_{inv}[a]	C—A—C	F—A—F	A	H—A—H	ΔE_{inv}[a]
N	107.2°	5.7	110.9°	102.4°	C	120.0°	0.0
P	93.4°	34.7	98.8°	97.2°	Si	112.7°	3.7
As	92.0°	39.7	96.2°	95.5°	Ge	112.4°	3.8
Sb	91.5°	44.9	94.2°	94.3°	Sn	110.6°	7.0
Bi	90.5°	60.5	97.1°	94.8°			

[a] C_{3v} to D_{3h} inversion barriers in kcal/mol.

them. The inversion barrier is, of course, the energy difference between the pyramidal and planar structures. The magnitude of the barrier is dictated by the slope of $2a_1$ in Figure 9.7; a steeper slope will yield a larger inversion barrier. Calculations [5] have consistently shown that upon decreasing the electronegativity of A, the pyramidal inversion barrier, ΔE_{inv}, increases and the HAH valence angle decreases. Table 9.1 presents several sets of data related to this for the eight-electron R_3A series where A runs down the group 15 column of the Periodic Table. The H_3A inversion barriers along with the F—A—F bond angles are derived from computations [6]. The H—A—H and C—A—C bond angles for the H_3A and Me_3A molecules are from microwave and electron diffraction measurements [7]. These observations are analogous to the corresponding ones in eight-electron AH_2 systems (Section 7.4.), and may be rationalized in terms of **9.12**. Geometry perturbation arguments point to the HOMO, $2a_1$, of pyramidal AH_3 as being constructed by the mixing of $2a_1'$ into a_2'' **(9.13)**. This orbital mixing stabilizes the

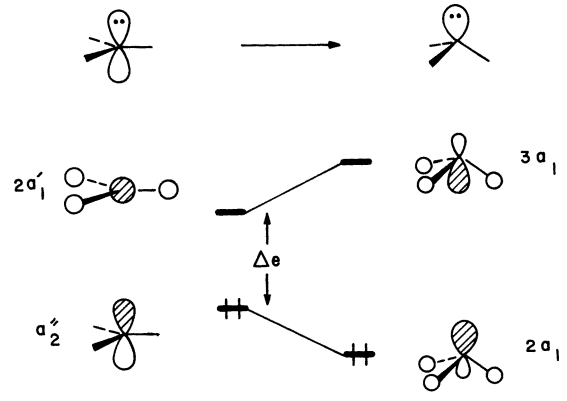

9.12

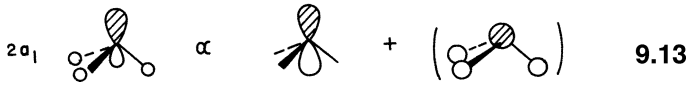

9.13

$2a_1$ level with respect to a_2''. The magnitude of the stabilization is inversely proportional to the energy gap, Δe, between the a_2'' and $2a_1'$ levels [4]. For exactly the same reasons as those discussed in Section 7.4B, the a_2'' and $2a_1'$ levels of planar AH_3 are raised and lowered in energy, respectively, as one goes down the Periodic Table for the group 15 elements. In other words, the a_2'' MO is raised in energy since the central atom is becoming less electronegative (see the state averaged ionization potential for the valence *p* AOs in **2.9**). For the N 2*s* and 2*p* AOs have comparable sizes but for the rest of the atoms in this series the valence *ns* AOs become

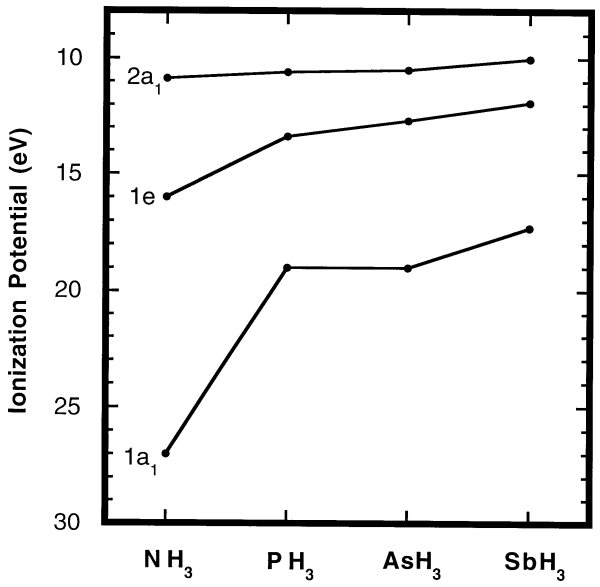

FIGURE 9.9
A plot of the vertical ionization potentials for the group 15 hydrides.

increasingly more contracted compared to the *np* AOs. The overlap then between the central *ns* AO and the hydrogen *s* orbitals decrease on going down the column, which results in the stabilization of the $2a_1'$ LUMO. Therefore, a smaller energy gap Δe, a larger inversion barrier, and a smaller HAH angle are found in eight-electron AH_3 systems as A becomes less electronegative. There is an interesting (and yet unexplained) inversion on going from Me_3Sb to Me_3Bi that is also present for F_3Bi (and I_3Bi [7]) but not H_3Bi.

The vertical ionization potentials for the NH_3 to SbH_3 series [8] are plotted in Figure 9.9. The $1a_1 - 1e$ energy differences going from NH_3 to SbH_3 are identical to the situation found for the $1a_1 - 1b_2$ energy separations in the group 16 AH_2 molecules, see Figure 7.10, or for the valence *s-p* energy gaps for the atoms in **2.9**. What is different is that for AH_2 the b_1 HOMO is found progressively at a lower ionization potential going down the column. On the other hand, for AH_3 the $2a_1$ MO is at a nearly constant ionization potential. The energy of the b_1 MO is invariant with respect to the H—A—H bond angle. However, the $2a_1$ MO decreases in energy when the H—A—H angle decreases (Figures 7.5 and 9.7). Since the H—A—H bond angle decreases going down the column for the group 15 molecules, there are two competing effects. The electronegativity decreases, which lowers the ionization potential, while the bond angle decreases, which should raise it. The net effect is one of near cancellation in the AH_3 series.

The above discussion also provides a rationale for the computational results that seven-electron AH_3 radicals with a first-row atom A (e.g., CH_3 and NH_3^+) are planar, but those with a second-row atom (e.g., SiH_3, GeH_3, and SnH_3) are pyramidal [9]. The a_2'' level is now only singly occupied and is of lower energy in the pyramidal geometry. However, the subjacent level, doubly degenerate and completely filled, is of lower energy at the planar geometry. A pyramidal structure is expected only if the energy lowering associated with a_2'' is substantial. This occurs for AH_3 systems containing a second-row atom A with a smaller electronegativity, and hence a smaller Δe value than their first-row counterparts. The results [9] for AH_3 are listed on the right side of Table 9.1. As expected from the arguments given above, the H—A—H angles are larger and the inversion barriers are smaller for the seven electron compounds compared to their eight electron counterparts. Furthermore, proceeding down the column for these group 14 molecules, the H—A—H bond angles become smaller and the inversion barriers larger, just like their group 15, eight-electron, counterparts.

9.4 π-BONDING EFFECTS OF LIGANDS

Let us consider AL_n ($n = 1, 2, 3, \ldots$) systems in which L refers to a "ligand," an atom or a group, that contains more than just a single *s* orbital. In most cases, L contributes one electron in a sigma fashion to A as shown in **9.14** for planar AL_3. The hybrid

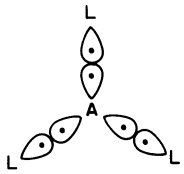

9.14

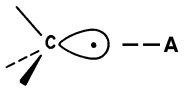

9.15

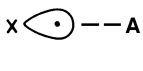

9.16

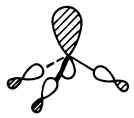

9.17

orbital used by L may be the sp^3 hybrid of an alkyl group in **9.15** or the *sp* hybrid of a halogen atom in **9.16**. The local symmetry of the hybrid orbitals in **9.15** or **9.16** is the same as that for a hydrogen *s* orbital. Thus, the way the atomic orbitals of A overlap with the ligand orbitals is the same whether the ligand carries a single *s* orbital or a directed (hybridized) orbital of this type. As a result, the overall shape and symmetry of the valence, A-centered orbitals of AL_n are the same as those of AH_n. The very important result is that the MOs of AH_n developed so far can be used to discuss the structures of AL_n systems where L is an arbitrary group (or groups). For example, the orbital of $N(CH_3)_3$ corresponding to the $2a_1$ orbital of pyramidal AH_3 is that shown in **9.17**. The hybrid orbitals on the methyl groups simply take the place of hydrogen *s* orbitals with the same relative phase as that for the $2a_1$ MO. There are two layers of detail that should be taken into account when dealing with groups other than hydrogen. First one should consider any electronegativity changes on going from hydrogen to L. Secondly, any π interactions that exist between L and A need to be turned on. It is normally prudent to carry out the perturbations in the order given. Electronegativity changes bring about alterations in the σ system of the molecule, whereas, π bonding is a smaller perturbation, which can easily be added in a secondary step. Let us pursue this construction for the eight-electron AH_3 case.

A very electronegative atom substituted at A causes all orbitals to decrease in energy (see Section 6.4), especially those that have appreciable orbital character associated with the electronegative substituent. There is a direct relationship between the energy lowering and the coefficients on the atoms that are made more electronegative. Consider the level ordering of planar, D_{3h} AH_3 in Figure 9.7. Replacement of the hydrogens by fluorine atoms would cause all of the MO levels to shift downward except for a_2'' (in reality the a_2'' orbital would also be slightly stabilized because of the increased Coulombic attraction by the electronegative fluorine atoms—see Section 8.9). The effect of π bonding between the central atom and the fluorine ligands as we shall shortly see will be to raise a_2'' in energy. Consequently, the energy gap Δe in **9.12** will be smaller for NF_3 than for NH_3. This suggests an explanation for the computational result that the NF_3 inversion barrier is larger (78.5 kcal/mol) and the F—N—F valence angle is smaller (102.4°—see Table 9.1) than the corresponding value for NH_3 (106.7°) [10]. The NF_3 inversion barrier of 78.5 kcal/mol via a D_{3h} structure is larger than the first bond dissociation energy of 57 kcal/mol so that bond breaking is energetically favored over distortion to the D_{3h} geometry. Instead inversion proceeds by a "T-shaped" transition state of C_{2v} symmetry [5]. The energy of the $2a_1'$ MO in the D_{3h} structure is now so low in energy that it can effectively mix with one component of the $1e'$ set. Therefore, the motion for inversion in NF_3, as well as the other group 15 fluorides, involves the

enlargement of one F—A—F bond angle. This couples the $2a_1$ MO with $1e_x$ (see Figure 9.4).

When the external ligand L is an atom or a group that possesses π-bonding capabilities it is convenient to separate the effects due to σ and π bonding. To do this, we first develop the valence orbitals around the central atom A, neglecting the π-bonding capabilities of L, and then introduce the π-bonding effects of L as a perturbation. As an example, consider H_2A-L where L stands for a group with a π-acceptor orbital ϕ_a (e.g., an empty p orbital of BH_2, that of an electropositive metal such as Li, or a π^*_{CO} orbital of a carbonyl group), which can engage in π interaction with the nonbonding orbital (analogous to a_2'') of A. The π interactions ($n_\pi - \phi_a$) and ($n_\sigma - \phi_a$) that occur in planar and pyramidal H_2A–L are shown in **9.18** and **9.19**,

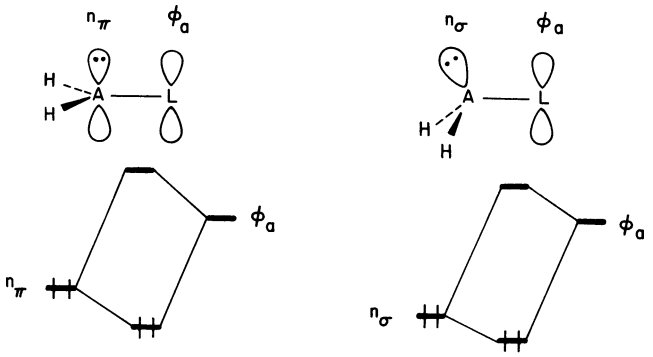

9.18 **9.19**

9.20

respectively. The stabilization of the nonbonding orbital on A is governed by the π overlap between the n and ϕ_a orbitals and by the energy gap Δe between them. As can be seen from **9.20**, the overlap $\langle n_\pi|\phi_a\rangle$ in **9.18** is greater than the overlap $\langle n_\sigma|\phi_a\rangle$ in **9.19**. Since the n_π level of AH_2 is higher in energy than the n_σ level, the energy gap Δe is smaller in **9.18**. Therefore, in terms of both overlap and energy gap considerations, the stabilization of n_π in **9.18** is greater than that of n_σ in **9.19**. Such a π interaction can stabilize the planar structure over the pyramidal one if it is larger than the competing σ-effect, described above, responsible for the pyramidal geometry of eight-electron AH_3 molecules. As shown for the ground state geometries in **9.21** and **9.22**, this is the case for H_2A-L with a first-row A atom but not for

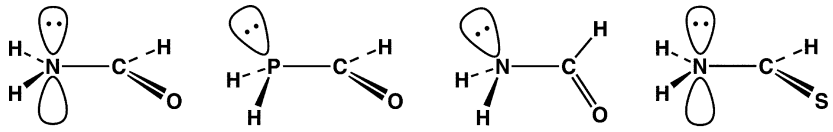

9.21 **9.22** **9.23** **9.24**

H_2A-L when a second-row A atom is present. For the case of the heavier A atom, although the energy gap Δe between n_π and ϕ_a is small, the $\langle n_\pi|\phi_a\rangle$ overlap is small too because of the longer A—L bond and more diffuse valence orbitals. In addition, recall that the inversion barrier of AH_3 is much larger for a second-

row atom compared to one from the first-row. As a result the $(n_\pi - \phi_a)$ interaction in **9.18** is not large enough to make H_2A-L planar when A comes from the second row [11,12]. It should be noted that the nitrogen center of **9.21** becomes pyramidal when the π interaction is cut off by rotation around the N—L bond as depicted in **9.23**. Thus, rotation about the C—N bond in amides or thioamides, **9.24**, is intimately coupled with inversion at the amide nitrogen [13]. The greater π acceptor capability of C=S compared to C=O leads to a stiffer out of plane wagging potential for the amino group in **9.24** compared to **9.21** and so thioformamide has a larger rotational barrier [13]. Likewise, rotation about the C—C bond in the enolate ion $^-$:$CH_2CH{=}O$ and that about the C—N bond in $^-$:CH_2NO_2 are calculated to be complicated by inversion at the carbanion center [14]. A similar situation occurs for the species $N(SiH_3)_3$ which has a planar NSi_3 skeleton, and $P(SiH_3)_3$ which has a pyramidal PSi_3 skeleton [11]. Here the acceptor orbital ϕ_a is one component of the 2e orbitals of SiH_3 (see Figure 9.4 and Section 10.5).

Consider now a molecule of the form H_2A-L, where L is a group with a π-donor function, ϕ_d (e.g., halogen atoms, a NH_2 or OR group, etc.). The result is opposite to that described above for the acceptor case. Here the effects of π and σ bonding work in the same direction (most σ donor groups contain an electronegative atom, e.g., N, O, Cl), and the barrier to inversion around the atom A is greater than that in the parent AH_3 system. As shown in **9.25** and **9.26**, the interaction between the nonbonding orbital of A and the donor orbital of L is a destabilizing two-orbital-four

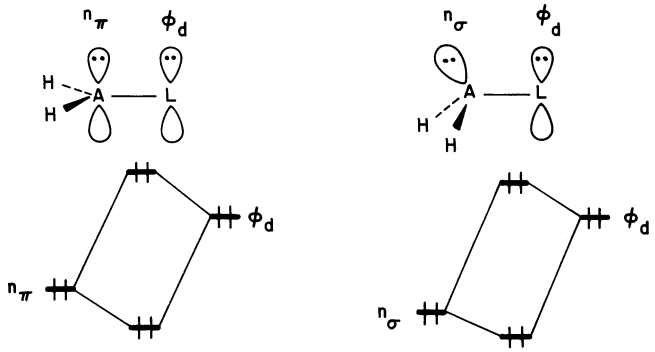

9.25 **9.26**

electron one. The destabilization is greater at the planar structure **9.25** since the overlap integral $\langle n_\pi | \phi_d \rangle$ is greater than $\langle n_\sigma | \phi_d \rangle$. Therefore, the π interaction between the A and L centers increases the inversion barrier. The effect of π acceptors and donors on bending in AH_2 (Section 7.3) can be understood in an identical fashion. This has a dramatic impact on not only the reactivity of carbenes but also the singlet-triplet energy difference (Section 8.10) [15]. Notice in the case of the singlet configuration that there is an acceptor orbital (b_2) and a donor orbital ($2a_1$) on the central atom. There is an interesting result, analogous to the observation concerning the planar skeleton of $N(SiH_3)_3$, in silicon–oxygen chemistry [16]. The average value of the Si—O—Si angle in silicates ($\sim$149°) lies between the linear and tetrahedral extremes. There is also evidence from the variety of angles known in such species that the bending around the oxygen is rather soft. Both of these observations may be interpreted in terms of Si—O π bonding, which best stabilizes the linear geometry while σ effects best stabilize a considerably nonlinear geometry.

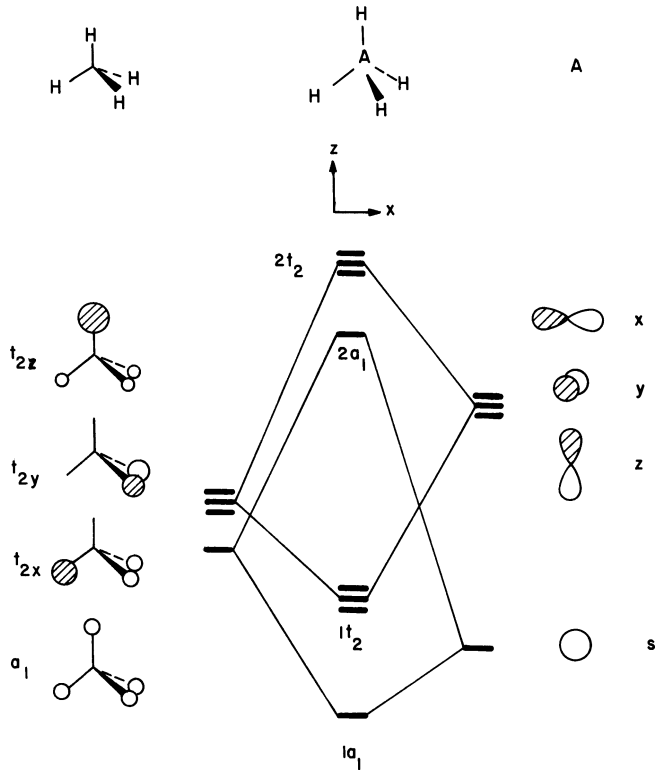

FIGURE 9.10
An orbital interaction diagram for tetrahedral AH_4.

9.5 THE AH_4 SYSTEM

The orbital interaction diagram between H_4 and A is shown in Figure 9.10. The triply degenerate MOs of tetrahedral H_4 are an alternative representation of those shown in Figure 5.6. The orbital interaction diagram of Figure 9.10 leads to the MOs of tetrahedral AH_4 shown in **9.27**. The a_1, t_{2x}, t_{2y}, and t_{2z} orbitals of H_4 combine in-phase with the s, p_x, p_y, and p_z orbitals of A to form the $1a_1$, $1t_{2x}$, $1t_{2y}$, and $1t_{2z}$ MOs.

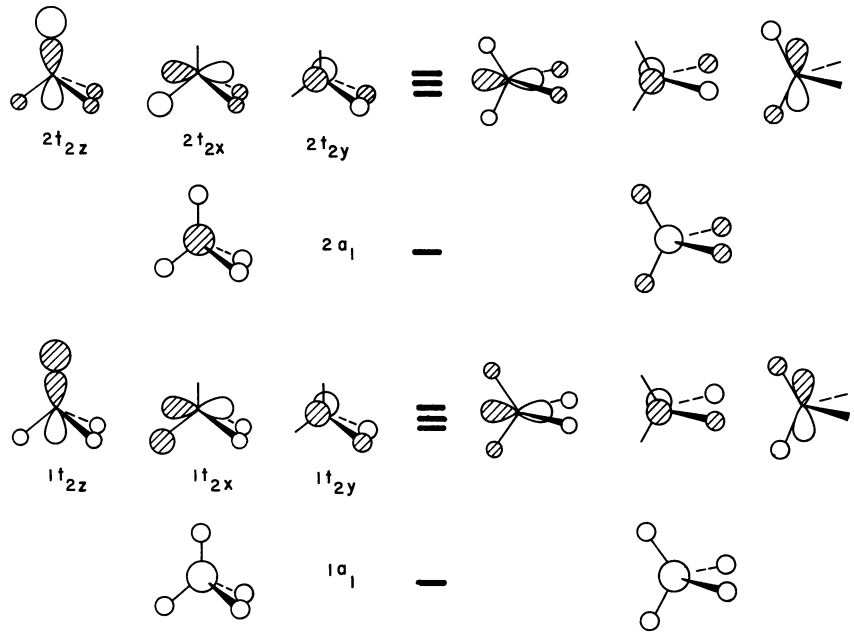

9.27 **9.28**

Likewise, the antibonding combination between the sets of fragment orbitals produces the $2a_1$, $2t_{2x}$, $2t_{2y}$, and $2t_{2z}$ MOs. With the MOs of tetrahedral H_4 chosen as in Figure 5.6, the MOs of AH_4 are given by **9.28**. We note that the triply degenerate MOs $1t_2$ or $2t_2$ of **9.28** can be expressed as linear combinations of the corresponding MOs of **9.27**. Such linear combinations among a set of degenerate MOs do not lift the degeneracy, as already pointed out in Section 7.4. One could take four sp^3 hybrid orbitals of A and interact them with the hydrogen s orbitals to form four σ_{AH} and four σ^*_{AH} orbitals. But these sets of four bond orbitals cannot all lie at the same energy (as we shall see in the next section from the PE spectra of CH_4 and SiH_4 molecules). Symmetry adaptation of the four σ_{AH} bond orbitals directly leads to the $1a_1$, $1t_{2x}$, $1t_{2y}$, and $1t_{2z}$ MOs as indicated in **9.29**. Similarly, the $2a_1$, $2t_{2x}$, $2t_{2y}$, and $2t_{2z}$ MOs can be well approximated by suitable linear combinations of the

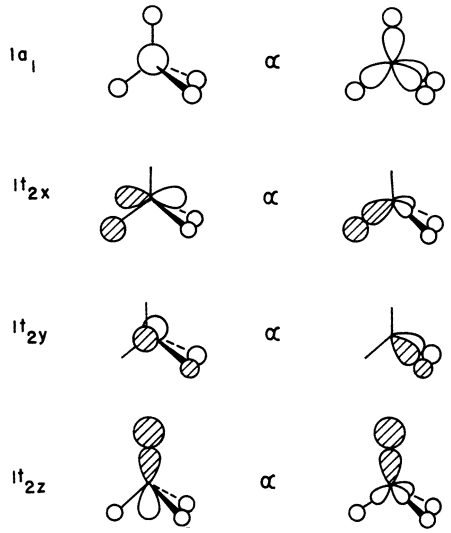

9.29

four σ^*_{AH} orbitals. Thus, symmetry adaptation of the bond orbitals directly leads to the delocalized MOs of tetrahedral AH_4 and, of course the totally symmetric a_1 combination no longer lies at the same energy as the t_2 set.

Figure 9.11 shows a Walsh diagram for opening two H—C—H angles in methane from the tetrahedral geometry ($\theta = 109.47^\circ$) to the square plane ($\theta = 180.0^\circ$). During the $T_d \rightarrow D_{4h}$ distortion, two members of the $1t_2$ set are stabilized, $e^{(1)} < 0$, since overlap between the p orbital on A and the two hydrogen s orbitals is increased and these are bonding MOs. But the third member is destabilized, $e^{(1)} > 0$, since all bonding between the p orbital of A and the hydrogen s orbitals is lost. This leads to the $1e_u$ and a_{2u} levels, respectively. For identical reasons, two members of the antibonding $2t_2$ set are destabilized and the third member is lowered in energy, yielding the $2e_u$ and b_{1g} levels. For the moment, we show the a_{2u} level lying below b_{1g} in Figure 9.11, but we note that the relative ordering of the two orbitals depends upon the electronegativity difference between A and H (or L) as will be discussed later. The $1a_1$ and $2a_1$ orbitals (not shown in Figure 9.11) do not change much in energy since they are constructed from s AOs on the central atom and the surrounding hydrogens and this overlap does not change much during the course of the deformation.

In eight-electron AH_4 systems such as CH_4 and NH_4^+, the HOMO of a square planar structure is the totally nonbonding a_{2u} level. Thus, according to Figure 9.11, an eight-electron AH_4 molecule prefers to be tetrahedral. The tetrahedral configuration of AH_4 may in principle be inverted as shown in **9.30**. However, the barrier for this inversion is exceedingly large compared with that for the pyramidal inversion in

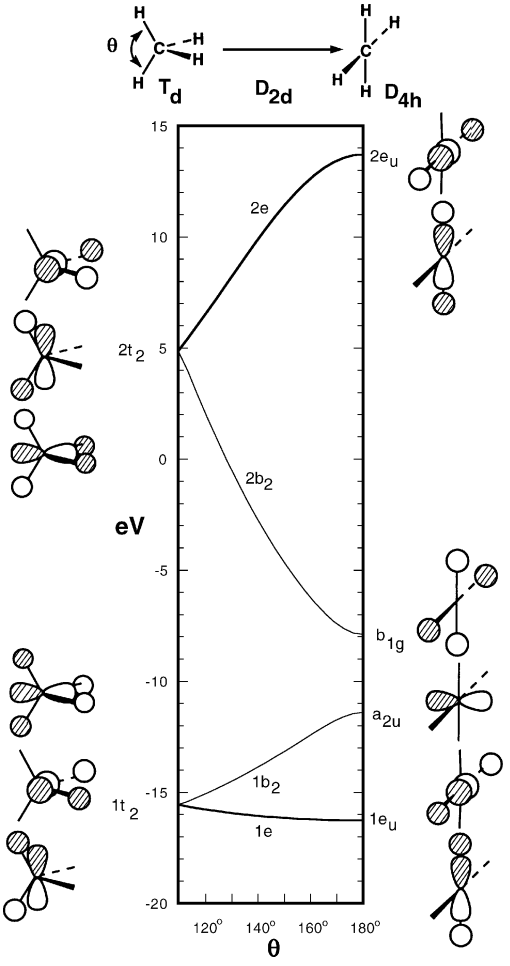

FIGURE 9.11

A Walsh diagram for bending two H—C—H bond angles in methane from the tetrahedral structure to the square planar one.

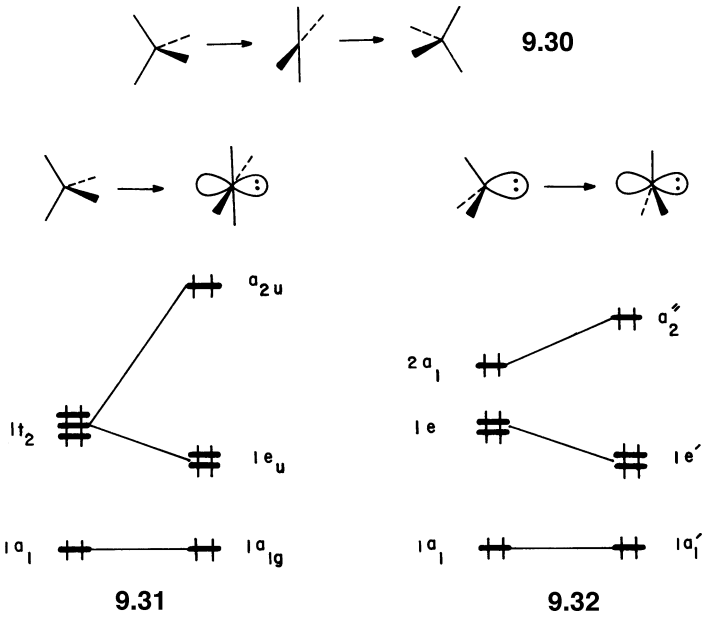

eight-electron AH_3 systems. For example, the energy difference between T_d and D_{4h} geometries in CH_4 is estimated to require about 131 kcal/mol from very high level calculations [17], in sharp contrast to the pyramidal inversion barrier of about 6 kcal/mol in NH_3 [5]. This observation may be understood by reference to **9.31** and **9.32**. What is largely responsible for the inversion barrier in AH_3 is the conversion of a nonbonding electron pair in a hybrid orbital ($2a_1$) into a pair in a pure p orbital. In contrast, the inversion of AH_4 requires the conversion of a bonding electron pair ($1t_2$) into a nonbonding electron pair in a p AO. This also brings up an interesting point concerning the square planar geometry for methane. Since the a_{2u} orbital is a pure p AO on carbon, pyramidalization should, just as in the eight electron AH_3 case, be stabilizing. The a_{2u} MO becomes hybridized on going to a C_{4v} geometry by mixing with the higher lying $2a_{1g}$ MO. This is indeed the case, the C_{4v} structure is 26 kcal/mol more stable than the D_{4h} one [17]. However, the actual structure for stereomutation of methane is predicted to be a pyramidal singlet carbene complexed to a hydrogen molecule with C_s symmetry. This structure is 1 kcal/mol lower in energy than the C_{4v} one. The H_2 unit is bound to the carbene by 13 kcal/mol but this structure is less stable than $CH_3^{\bullet}$ and $H^{\bullet}$ by 3 kcal/mol [17]. So stereomutation of methane without bond rupture is not likely to occur.

A square planar carbon configuration can be achieved only if the HOMO a_{2u} is substantially stabilized by good π-acceptor ligands. For example, di- and trilithiomethane are calculated to have a planar structure **9.33a** only 2.5 and 3.5 kcal/mol, respectively, higher than the tetrahedral structures **9.33b** [18]. As indicated in **9.33c**,

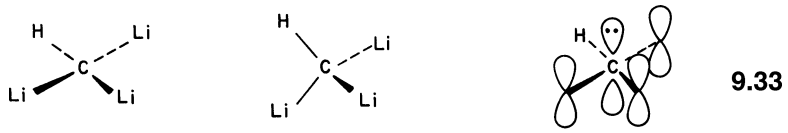

9.33

a **b** **c**

the low-lying empty p orbitals of Li stabilize the two electrons in the a_{2u} orbital. Similarly, the eight-electron Li_2O is not bent like H_2O but linear in structure. However, Cs_2O is bent although it is isoelectronic with Li_2O [19], because the magnitude of π overlap associated with the p orbital of a heavier element is much weaker. Recall from Section 9.4 that the nitrogen center of $H_2NCH{=}O$ is planar while the phosphorus center of $H_2PCH{=}O$ is pyramidal.

As the electronegativity of A in an AH_4 molecule is decreased, the p orbital of A is raised in energy and the A–H distance tends to increase. Furthermore, the $1t_2$ set becomes more concentrated on the hydrogens, and $2t_2$ more concentrated on A. Consequently, in a square planar AH_4 molecule with an electropositive atom, b_{1g} may become lower in energy than a_{2u}. As shown in **9.34** there is actually an avoided crossing between the two MOs which eventually become a_{2u} and b_{1g} at the D_{4h}

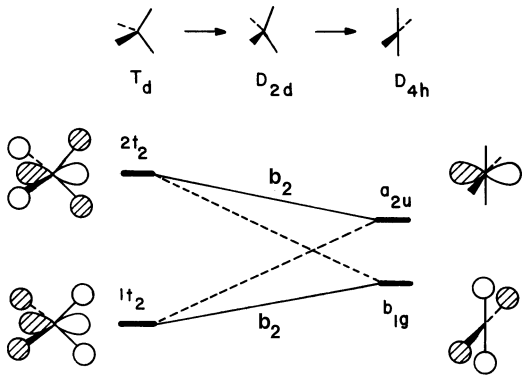

9.34

geometry. At intermediate geometries they both have b_2 symmetry and can intermix. In fact, the HOMO of a square planar BH_4^-, SiH_4, or PH_4^+ molecule is calculated to be the b_{1g} level [20]. One important consequence of such a level ordering is that AL_4 systems with electronegative ligands such as halogens or alkoxides should have a lower barrier for configuration inversion at A than CH_4. This comes about because the HOMO b_{1g} carries electron density only on the ligand atoms, and will be stabilized by electronegative atoms. In addition, electronegative atoms carry nonbonding electron pairs. A two-orbital-two-electron stabilization results via interaction with the central atom p orbital (a_{2u}) of the planar structure as depicted in **9.35**. Square planar oxygen is known in the solid-state structure of

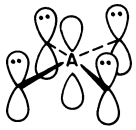

9.35

NbO and TiO [21]. Here the square planar geometry is stabilized by the presence of π-acceptor Nb (or Ti) d orbitals. Likewise, molecules in which a_{2u} is empty are expected to be more stable at the square planar rather than tetrahedral or C_{4v} pyramidal geometry. Examples include BH_4^+, CH_4^{2+}, or the doubly excited state of CH_4 in which a_{2u} is empty and b_{1g} is filled [22]. We will return to this problem of tetrahedral-square planar-C_{4v} pyramidal structure interconversion in Chapter 14, where AL_4 molecules with more than eight electrons are considered.

Actually a C_{2v} structure for CH_4^{2+} has been found from high-level calculations [23] to be 1 kcal/mol more stable than the D_{4h} one. It structurally resembles a methylene dication coordinated to an H_2 ligand. The H—H distance was found to be 1.03 Å [23], which is elongated compared to the hydrogen molecule at 0.74 Å and the C—H distance (to the H_2 group) was 1.28 Å. It is instructive to look more closely at the bonding in this structure from the perspective of a CH_2^{2+} species coordinated to H_2. This is done for the ground state structure of CH_4^{2+} in Figure 9.12a. Here the b_1 and $2a_1$ frontier orbitals of the CH_2^{2+} fragment are

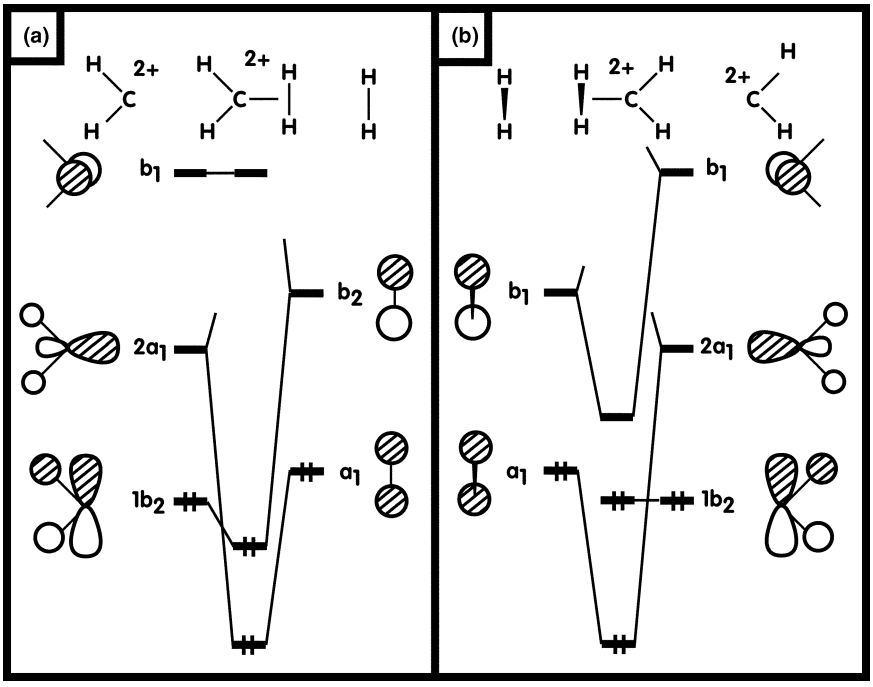

FIGURE 9.12
An orbital interaction diagram for CH_4^{2+} (a) in the ground state and (b) a rotational transition state, where H_2 lies perpendicular to the CH_2 plane.

empty. The $2a_1$ fragment orbital interacts and stabilizes the filled σ orbital of H_2. The b_1 fragment orbital is left nonbonding since the H_2 and CH_2^{2+} units lie in a common plane in this structure. So electron density from the filled H_2 σ orbital is now delocalized over three centers and the $2a_1$ fragment orbital becomes partly occupied. A CH_2^{2+} molecule with four valence electrons is predicted to be linear (see Section 7.3). Here the H—C—H angle closes down to 124.1°. It lies midway between the value expected (180°) for an isolated CH_2^{2+} molecule and that (90°) for the square planar compound as a consequence of the partial occupation of $2a_1$. But there is also a π interaction between the filled C—H σ bonding orbital, $1b_2$, and the empty H_2 σ^* orbital. This would be called back-donation by some and the $2a_1$-H_2 σ interaction, forward-donation. Back-donation here takes electron density from the CH_2^{2+} unit and places it in H_2 σ^*. The structural consequence of this is to elongate the H—H bond and shorten the C—H bonds (to the H_2 ligand). Thus, if back-donation were made more important, then the D_{4h} geometry for CH_4^{2+} where the H—H bond is completely broken would become the ground state. Now suppose one rotates the H_2 ligand by 90° to another C_{2v} structure, which is analyzed in Figure 9.12b. The H_2 σ orbital is involved in the same interaction and is stabilized by an identical amount since the $2a_1$ fragment acceptor orbital is cylindrically symmetrical. In other words, the $2a_1$–H_2 σ overlap is identical in both conformations. What is different is that now H_2 σ^* has b_1 symmetry and it interacts with the empty b_1 fragment orbital on CH_2^{2+}. The bonding combination is not filled so this has no energetic impact. There is no longer any back-donation. As a consequence this structure was found [23] to be 13 kcal/mol higher in energy than the ground state one. The H—H distance was much smaller —0.90 Å and the C—H distance (to H_2) of 1.43 Å was longer than that found in the ground state. So the absence of back-donation makes the H_2 ligand less strongly bound. Now with two more electrons, the b_1 fragment orbital on CH_2 is filled and its interaction with H_2 σ^* is strongly stabilizing so the H—H bond is broken and the tetrahedral geometry becomes the ground state. This brings up the result [17] mentioned previously for planar CH_4. A CH_2 fragment will have $2a_1$ filled and b_1 empty. Therefore, H_2 σ can only interact in a stabilizing fashion with b_1, which precisely corresponds to the geometry found in the calculations. There is no back-donation so the H—H distance is again rather short at 0.88 Å [17]. We shall return to a related problem, the coordination of AH_3^+ to H_2, in Section 14.3.

9.6 THE AH_n SERIES—SOME GENERALIZATIONS

There are many connections between the molecular orbitals of the AH_n series that we have studied here and in Chapter 7. One could build a generalized orbital interaction consisting of the *s* and three *p* AOs on A. When symmetry adapted combinations of the *n* (where $n \leq 4$) *s* AOs on the hydrogen atoms are made, *n* A–H (delocalized) stabilized bonding MOs are produced. There will also be *n* A–H antibonding orbitals at high energy. Left behind are 4-*n* nonbonding MOs, which are localized on the central atom. Thus, when $n = 2$, there are two bonding and antibonding A–H orbitals. Left behind are the two nonbonding MOs (the $1\pi_u$ set for linear molecules or $2a_1$ and b_1 for bent ones—see Section 7.1). One rule of thumb that we will use extensively is that a stable molecule (in a thermodynamic sense) will be one where all bonding MOs are filled. The nonbonding orbitals will be filled in this case if the central atom is electronegative; they lie at low energies. Therefore, a total of $2 \times [(n) + (4 - n)] = 8$ electrons will lead to a stable molecule.

This is a very roundabout way to derive the eight electron rare-gas rule. As we will see in Section 14.1 an extension of this offers a particularly simple way to view the so-called hypervalent molecules and electron counting in organometallic molecules in later chapters.

Another way to view the AH_n series can be developed as follows: in tetrahedral AH_4 the four atomic orbitals of A find a one-to-one match with the four orbitals of tetrahedral H_4. Consequently four bonding and four antibonding MOs are produced. One hydrogen atom can be removed from AH_4 to produce pyramidal AH_3. This produces a nonbonding orbital localized on A. The three bonding and three antibonding MOs of AH_3 have an essentially identical composition to their counterparts in AH_4. Likewise, in AH_2 two hydrogen atoms have been removed which creates two A-centered nonbonding orbitals. Two A—H bonding and two A—H antibonding orbitals that are remnants of those in AH_4 remain. In AH there are three A-centered nonbonding orbitals and only one A—H bonding and one A—H antibonding MO. Therefore, each time a hydrogen atom is removed from a bonding orbital, this MO will rise in energy. This can be dramatically illustrated for the AH_n series by photoelectron spectroscopy. Figure 9.13 presents the relevant

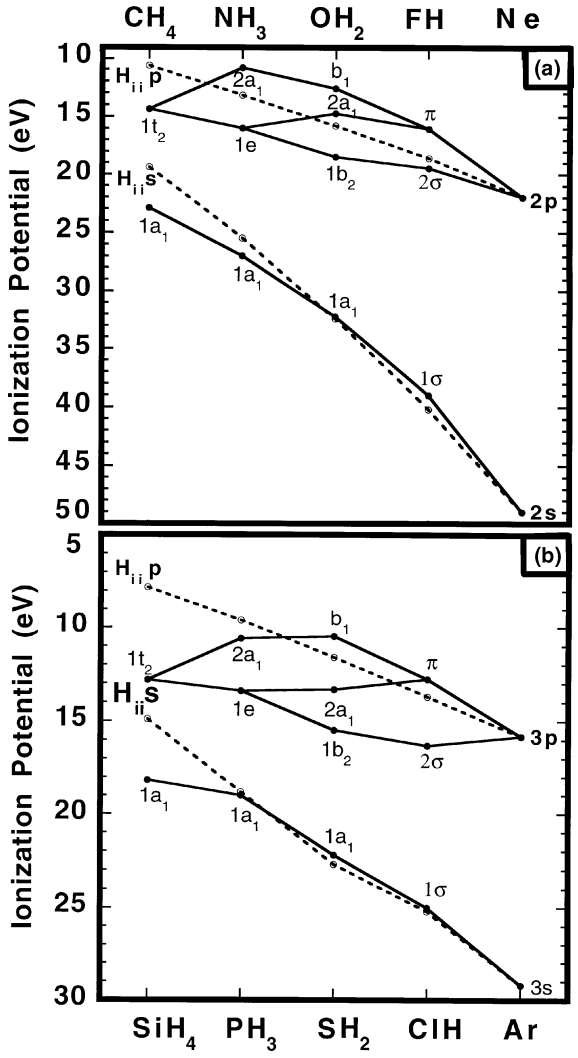

FIGURE 9.13

Plot of the vertical ionization potentials for the eight electron AH_4, AH_3, AH_2, AH, and A series. First row molecules are plotted in (a) and second row ones in (b). The dotted line indicates the state averaged ionization potentials for the A atoms.

data [24] in terms of a graph. Figure 9.13a plots the vertical ionization potentials of CH_4, NH_3, H_2O, HF, and Ne. Figure 9.13b does the same for the SiH_4 to Ar series from the second row of the Periodic Table. Notice that the energy scale is more expanded in Figure 9.13b than it is in Figure 9.13a. On going from CH_4 to NH_3 (or SiH_4 to PH_3) one member of the $1t_2$ set is destabilized to become the nonbonding $2a_1$ MO. Now the electronegativity of N is much greater than that of C so the bonding 1e set lies lower in energy than $1t_2$ and, of course, $1a_1$ in NH_3 is lower in energy than $1a_1$ in CH_4. In other words, using electronegativity perturbation theory considerations (Section 6.4) $e^{(1)} < 0$ for these transformations. On going from NH_3 to H_2O one member of the N—H bonding 1e set is destabilized to create the nonbonding $2a_1$ MO. Finally going from H_2O to HF, the $1b_2$ A—H bonding MO is not destabilized, but is actually stabilized by 1 eV on going to the nonbonding 2σ MO in HF. However, this is much less than the stabilization on going from $1a_1$ to 1σ (6.8 eV) which is due to the increased electronegativity of F compared to O. Note that on moving from the nonbonding but hybridized $2a_1$ orbital in PH_3 to the b_1 MO in H_2S, solely a p AO on S, the ionization potential decreases. This does not quite happen for the NH_3 to H_2O transformation because the electronegativity difference between N and O is much larger than that between P and S, see Figure 2.4. A feeling of the energetic impact of electronegativity on the MO energies can be appreciated by plotting the state-averaged ionization potentials for the central atoms (from **2.9**). These are the dashed lines in Figure 9.13. One might think that since these are a measure of the energy of an electron in an atomic orbital associated with an atom, then it should be easy to tell how much stabilization ensues when the hydrogen atoms interact with the central atom. In part this is true, but then only in a qualitative sense. In CH_4 and SiH_4 the $1a_1$ and $1t_2$ MOs are stabilized by a healthy amount with respect to the s and p H_{ii}s of C and Si. But then the H_{ii} values for the s valence orbitals are almost coincident with the $1a_1$ (and 1σ) MOs for the remaining molecules. Certainly on going from the left to the right of this series, the lowest MO becomes increasingly concentrated on the central atom since it becomes more and more electronegative compared to hydrogen. But this is not the whole story. Note that the b_1 and π MOs for both rows have ionization potentials that are lower in energy than their H_{ii} p AO atomic counterparts, yet these MOs are precisely a p AO on the central atom! The reason for this is increased electron–electron repulsion in the molecules compared to the atoms. Consider the oxygen atom, which has a s^2p^4 electron configuration. The state averaged ionization potential then is one where four electrons are arranged in some (high spin) manner around three p AOs. So the average electron occupancy per p AO is <2. Contrast this situation with the b_1 MO in H_2O. Here the b_1 MO of course is occupied with two electrons and these electrons are paired. So there is a greater Coulomb repulsion energy, and pairing the electrons in b_1 also raises their energy (see Sections 8.8 and 8.9). Consistent with this explanation is that the differences are smaller for the second row (see Figure 9.13b). Here the orbitals on the central atoms are more diffuse so the differences in Coulomb repulsion and the pairing energies are smaller. The dashed lines for the p AOs do nicely divide bonding from nonbonding regions and both dashed lines do reflect the electronegativity perturbations brought about by the different atoms. But to emphasize again the value of Figure 9.13 we have here an experimental demonstration of the conversion of bonding into nonbonding MOs by removal of hydrogen atoms. This reductive approach for determining the valence orbitals of AH_n species will be extended greatly when we discuss the ML_n transition metal fragment series. Very similar patterns will emerge.

PROBLEMS

9.1. **a.** Construct a Walsh diagram for the distortion shown below.

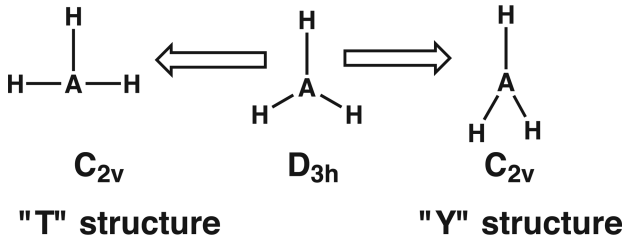

b. Predict what electron count(s) are viable for either C_{2v} geometry.

c. The optimum geometry for LiH_3 is calculated to be the C_{2v} "T" structure. Use the Jahn–Teller theorem to show that it anticipates the distortion from D_{3h} to this structure.

d. Predict the reaction path for the rearrangement shown below.

9.2. Explain the following experimental facts:

H—A—H angles: CH_3^-, 105°; NH_3, 106.7°; OH_3^+, 110°.

H_3A inversion barriers: CH_3^-, 8 kcal/mol; NH_3, 5.8 kcal/mol; OH_3^+, 2 kcal/mol.

9.3. CH_4^{2+} is a known molecule but its structure has not been established by experiment. The structure as determined by high-level calculations was discussed in Problem 7.5. In this problem, we study possible geometries derived from a "gedankenexperiment" using the Jahn–Teller theorem and constructing Walsh diagrams using geometric perturbation theory.

a. The MOs of tetrahedral AH_4 are drawn out in **9.27** and **9.28**. For CH_4^{2+} the orbital occupancy will be $(1a_1)^2(1t_2)^4$. Use the Jahn–Teller theorem and the normal modes for an AB_4 tetrahedral molecule in Appendix III to predict possible geometries for CH_4^{2+}.

b. Construct Walsh diagrams for all of the possible distortions and predict possible stable structures.

9.4. We see in Section 21.5 that a R_3P-Au fragment has very similar bonding properties compared to a hydrogen atom! Construct an orbital interaction diagram for H_3P-Au by interacting the HOMO of PH_3 (which has an ionization potential of 10.0 eV) with the *s* and *p* AOs of Au (*s* and *p* $H_{ii} = -10.9$ and -5.6 eV, respectively). The *d* AOs of Au lie a very low energy and to a first approximation will not mix too heavily into the other MOs. Draw out the resultant MOs and indicate the orbital occupancy.

9.5. **a.** There are three possible geometries for hydroxylamine as shown below. Using the ideas from **9.26** determine the relative order of stabilities for these three conformations.

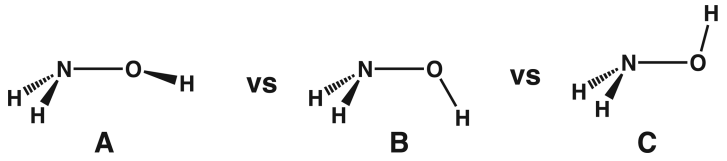

b. The photoelectron spectrum of hydroxylamine is shown below as adapted from Reference [25]. Using the PE spectral data for water in Figure 7.9 and ammonia in Figure 9.9 assign the five ionizations for NH_2OH.

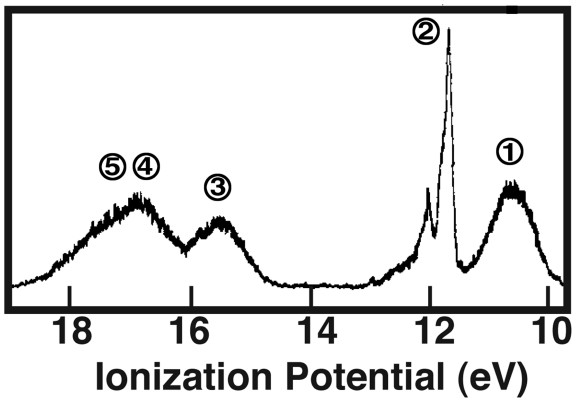

REFERENCES

1. B. M. Gimarc, *Molecular Structure and Bonding*, Academic Press, New York (1979).
2. A. D. Walsh, *J. Chem. Soc.*, 2266, 2288, 2296, 2301, 2306, 2318, 2321, 2325, 2330, 2260, (1953).
3. C. C. Levin, *J. Am. Chem. Soc.*, **97**, 5649 (1975).
4. B. M. Gimarc, *J. Am. Chem. Soc.*, **95**, 1417 (1973); A careful, rigorous treatment may be found in M. Atanasov and D. Reinen, *J. Am. Chem. Soc.*, **105**, 5450 (2001).
5. D. A. Dixon and D. S. Marynick, *J. Am. Chem. Soc.*, **99**, 6101 (1977); P. Schwerdtfeger, P. D. W. Boyd, T. Fischer, P. Hunt, and M. Liddell, *J. Am. Chem. Soc.*, **116**, 9620 (1994); P. Schwerdtfeger, L. J. Laakkonen, and P. Pyykkö, *J. Chem. Phys.*, **96**, 6807 (1992).
6. J. Moc and K. Morokuma, *Inorg. Chem.*, **33**, 551 (1994).
7. P Helminger, F. C.De Lucia, W. Gordy, H. W. Morgan, and P. A. Staats, *Phys. Rev.*, **9**, 12 (1974); K. Kijima and T. Tanaka, *J. Mol. Spectrosc..*, **89**, **62** (1981); M. Carlotti, G. DiLonardo, and L. Fusina, *J. Mol. Spectrosc.*, **102**, 310 (1983); W. Jeerzembeck, H. Büger, L. Constantin, L. Margules, J. Demaison, J. Breidung, and W. Thiel, *Angew. Chem. Int. Ed.*, **41**, 2550 (2002); B. Beagley and A. R. Medwid, *J. Mol. Struct.*, **38**, 229 (1977); J. Molnár, M. Kolonits, M. Hargittai, R. J. M. Konings, and A. S. Booij, *Inorg. Chem.*, **35**, 7639 (1996).
8. A. W. Potts and W. C. Price, *Proc. R. Soc. Lond. A*, **326**, 181 (1972).
9. T. A. Claxton and N. A. Smith, *J. Chem. Phys.*, **52**, 4317 (1970); F. Matthias, T. Ziegler, and P. v. R. Schleyer, *Organometallics*, **15**, 1477 (1996).
10. D. S. Marynick, *J. Chem. Phys.*, **73**, 3939 (1980).
11. K. Mislow, *Trans. N. Y. Acad. Sci.*, **35**, 227 (1973).
12. D. E. Dougherty, K. Mislow, and M.-H. Whangbo, *Tetrahedron Lett.*, **2321** (1979); J. R. Damewood, Jr. and K. Mislow, *Monatshefte für Chemie*, **111**, 213 (1980).
13. V. J. Klimkowski, H. L. Sellers, and L. Schafer, *J. Mol. Struct.*, **54**, 299 (1979); K. B. Wiberg and P. R. Rablen, *J. Am. Chem. Soc.*, **117**, 2201 (1995); K. B. Wiberg, P. R. Rablen, D. J. Rush, and T. A. Keith, *J. Am. Chem. Soc.*, **117**, 4261 (1995).
14. S. Wolfe, H. B. Schlegel, I. G. Csizmadia, and F. Bernardi, *Can. J. Chem.*, **53**, 3365 (1975); P. G. Mezey, A. Kresge, and I. G. Csizmadia, *Can. J. Chem.*, **54**, 2526 (1976); See also A. M. El-Nahas and P. v. R. Schleyer, *J. Comp. Chem.*, **15**, 596 (1994) for a number of related examples.
15. R. A. Moss, W. Guo, D. Z. Denny, K. N. Houk, and N. G. Rondan, *J. Am. Chem. Soc.*, **103**, 6164 (1981); P. H. Mueller, N. G. Rondan, K. N. Houk, J. F. Harrison, D. Hooper, B. H. Willen, and J. F. Liebman, *J. Am. Chem. Soc.*, **103**, 5049 (1981); N. G. Rondan, K. N. Houk, and R. A. Moss, *J. Am. Chem. Soc.*, **102**, 1770 (1980).

16. G. V. Gibbs, E. P. Meagher, M. B. Newton, and D. K. Swanson, *Structure and Bonding in Crystals*, Vol. **1**, M. O'Keeffe and A. Navrotsky, editors, Academic Press, New York p. 195. (1981).
17. M. J. M. Pepper, I. Shavitt, P. v. R. Schleyer, M. N. Glukhovtsev, R. Janochek, and M. Quack, *J. Comp. Chem.*, **16**, 207 (1995).
18. T. Clark and P. v. R. Schleyer, *J. Am. Chem. Soc.*, **101**, 7747 (1979); K. Sorger and P. v. R. Schleyer, *J. Mol. Struct. (Theochem)*, **338**, 317 (1995).
19. A. F. Wells, *Structural Inogranic Chemistry*, 4th edition, Clarendon, Oxford (1975).
20. M.-B. Krogh-Jespersen, J. Chandrasekhar, E.-U. Wurthwein, J. B. Collins, and P. v. R. Schleyer, *J. Am. Chem. Soc.*, **102**, 2263 (1980).
21. J. K. Burdett and T. Hughbanks, *J. Am. Chem. Soc.*, **106**, 3101 (1984).
22. J. B. Collins, P. v. R. Schleyer, J. S. Binkley, J. A. Pople, and L. Radom, *J. Am. Chem. Soc.*, **98**, 3436 (1976).
23. M. W. Wong and L. Radom, *J. Am. Chem. Soc.*, **111**, 1155 (1989).
24. A. W. Potts and W. C. Price, *Proc. R. Soc. Lond. A.*, **326**, 165, 181 (1972).
25. K. Kimura and S. Katsumata, *J. Chem. Phys.*, **67**, 1225 (1977)